

An investigation of flare emissions at multiple wavelengths

Dong Li^{1,2,3*}, Alexander Warmuth⁴, Lei Lu¹, and Zongjun Ning^{1,5}

¹Key Laboratory for Dark Matter and Space Science, Purple Mountain Observatory, CAS, Nanjing 210033, China; lidong@pmo.ac.cn

²CAS Key Laboratory of Solar Activity, National Astronomical Observatories, Beijing 100101, China

³State Key Laboratory of Space Weather, Chinese Academy of Sciences, Beijing 100190, China

⁴Leibniz-Institut für Astrophysik Potsdam (AIP), An der Sternwarte 16, 14482 Potsdam, Germany

⁵School of Astronomy and Space Science, University of Science and Technology of China, Hefei 230026, China

Abstract We report multi-wavelength observations of four solar flares on 2014 July 07. We firstly select these flares according to the soft X-ray (SXR) and extreme ultraviolet (EUV) emissions recorded by the Extreme Ultraviolet Variability Experiment and Geostationary Orbiting Environmental Satellites. Then their locations and geometries are identified from the full-disk images measured by the Atmospheric Imaging Assembly (AIA), and the time delays among the light curves in different channels are identified. The electron number densities are estimated using the Differential Emission Measure method. We find that three of four flares show strong emissions in SXR channels and high temperature (>6 MK) EUV wavelengths during the impulsive phase, i.e., AIA 131 Å and 94 Å, and then they emit peak radiation subsequently in the middle temperature (~ 0.6 – 3 MK) EUV channels. Moreover, they last for a long time and have smaller electron densities, which are probably driven by the interaction of hot diffuse flare loops. Only one flare emits radiation at almost the same time in all the observed wavelengths, lasts for a relatively short time, and has a larger electron density. It is also accompanied by a type III radio burst. The bright emission at the EUV channel could be corresponding to the associated erupting filament.

Key words: Sun: flares – Sun: radio radiation – Sun: UV radiation – Sun: X-rays, gamma rays

1 INTRODUCTION

Solar flare represents an impulsive and explosive release of magnetic free energy by reconnection, which is always characterized by a complex magnetic geometry (Masuda et al., 1994; Shibata et al., 1995; Priest & Forbes, 2002; Chen et al., 2020). The wavelength regime at which flares radiate is very wide, ranging from radio through optical and extreme ultraviolet (EUV) to soft/hard X-ray (SXR/HXR) and even γ -rays beyond 1 GeV (e.g., Fletcher et al., 2011; Benz, 2017). In a typical solar flare, a large amount of magnetic free energy is released via magnetic reconnection in the corona (Shibata & Magara, 2011; Li et al., 2016; Xue et al., 2016), e. g. as described in the 2-D reconnection model (Sturrock & Coppi, 1964) or the CSHKP model (Carmichael, 1964; Sturrock, 1966; Hirayama,

* Supported by the National Natural Science Foundation of China.

* Corresponding author

1974; Kopp & Pneuman, 1976). In this process, plasma will be heated to more than 10 MK in the reconnection region, and electrons will be efficiently accelerated to nonthermal energies. Subsequently, the released energy will be transported away from the reconnection site in the form of bi-directional outflows (e.g., Wang et al., 2007; Mann & Warmuth, 2011; Liu et al., 2013; Li, 2019; Ning et al., 2020). A fraction of the energy will be transported down to the transition region and chromosphere or even photosphere along the newly formed flare loops via thermal conduction and/or nonthermal electrons (Priest & Forbes, 2000; Battaglia et al., 2009; Warmuth & Mann, 2016; Emslie & Bian, 2018). During this process, the flare loops can be clearly seen in SXR and EUV wavelengths (Sui & Holman, 2003; Krucker et al., 2008; Qiu et al., 2009; Yan et al., 2018), and double footpoints at the loop-legs and one or two loop-top sources can be produced in HXR or microwave channels (e.g., Fletcher & Hudson, 2002; Lin et al., 2003; Asai et al., 2006; Chen et al., 2017), while the flare ribbons are formed in $H\alpha$, visible, UV, and EUV wavebands (Temmer et al., 2007; Wang et al., 2014; Milligan, 2015; Li et al., 2017a; Song et al., 2018). Then the dense material in the low solar atmosphere is rapidly heated to more than 10 MK and the resulting overpressure causes an upward bulk flow along the flare loops at a fast speed, which is termed ‘chromospheric evaporation’ (Fisher et al., 1985; Brosius et al., 2016; Li et al., 2017b; Tian & Chen, 2018). At the same time, some of the released energy might travel up to the outer corona or the interplanetary space in the form of nonthermal electrons, which might produce type III radio bursts. Usually, coronal mass ejections (CMEs) may also be accompanied by solar flares (Lin et al., 2005; Zhang et al., 2010; Cheng et al., 2018).

There are different classification schemes for solar flares. The GOES class is a measurement of flare importance based on the peak SXR 1–8 Å flux measured by the Geostationary Orbiting Environmental Satellites (GOES, Thomas & Teske, 1971; Fletcher et al., 2011). At a single wavelength, such as a SXR, HXR or radio channel, the temporal evolution of the irradiance of a solar flare might be characterized as either impulsive or gradual (Pallavicini et al., 1977; Ohki et al., 1983). This has to be distinguished from the evolutionary phases of a solar flare, which are defined according to specific characteristics of the emission, i.e., pre-flare phase, impulsive phase, and decay phase (Hoyng et al., 1981; Benz, 2017). Still another classification scheme considers the geometric properties of flares, which is an important aspect since it reflects the underlying magnetic topology. Accordingly, flares may display double or multiple ribbons, circular ribbons, or might be very compact, which can be clearly seen in $H\alpha$, UV or EUV images (see., Saint-Hilaire & Benz, 2002; Su et al., 2007; Radziszewski et al., 2007; Zhang et al., 2020). Conversely, multiple loops and footpoints are easily observed in X-ray, EUV or radio images (Masuda et al., 1994; Su et al., 2013; Chen et al., 2017). Solar flares can also be considered as either eruptive or confined (e.g., Svestka & Cliver, 1992; Priest & Forbes, 2002; Ji et al., 2003; Wang & Zhang, 2007; Shen et al., 2011). The eruptive flares are often associated with the filament eruptions, CMEs, and/or other ejecta (Lin, 2004; Forbes et al., 2006; Cheng et al., 2018), while the latter events are mostly caused by complex flare loop structures (e.g., Fan & Gibson, 2007; Guo et al., 2010; Yang et al., 2014; Zhang et al., 2017). Finally, a second peak of warm coronal emissions (e.g., Fe xvii 335 Å) are found in solar flares and named as the EUV late phase, which is separated from the primary SXR peak by tens of minutes or even a few hours (Woods et al., 2011). Observations show that the EUV late phase flare often shows double warm EUV peaks but only one SXR peak. The warm EUV emission in the late phase is suggested to be originated from a set of large-scale loops that are longer and higher than the primary loops in the main phase of solar flare. It is thought to be related to long-lasting cooling or additional heating (e.g., Dai et al., 2013; Li et al., 2014; Woods, 2014; Liu et al., 2015, and references therein).

Multi-wavelength observations of solar flares can provide an opportunity to improve our understanding of the flare model. In this paper, we performed a detailed analysis of four solar flares occurring on 2014 July 07, which were simultaneously observed by the GOES SXR channels, the Atmospheric Imaging Assembly (AIA, Lemen et al., 2012) and Extreme Ultraviolet Variability Experiment (EVE, Woods et al., 2012) aboard Solar Dynamics Observatory (SDO) in SXR and EUV wavelengths, and the SWAVES instruments (Kaiser et al., 2008) onboard Solar Terrestrial Relations Observatory Behind (STEREO.B). We mainly focused on the wavelength range over which the flare was emitting and on their decay time in EUV wavelengths and tried to search the causes of different emission characteris-

Table 1 The details of the observational instruments in this paper

| Instruments | Channels | Cadence (s) | Descriptions |
|-------------|------------------|-------------|--------------|
| GOES | 1–8 Å | ~2.0 | SXR |
| | 0.5–4 Å | ~2.0 | SXR |
| SWAVES | 0.023–16.025 MHz | 60.0 | radio |
| SDO/AIA | 94 Å–335 Å | 24.0 | EUV |
| SDO/EVE/ESP | 1–70 Å | 0.25 | SXR |
| | 180 Å | 0.25 | 172–206 Å |
| | 300 Å | 0.25 | 280–316 Å |

tics of solar flares at multiple wavelengths. This paper is organized as following: the observations are introduced in Section 2, and the results are given in Section 3, then our conclusions and discussions are presented in Section 4.

2 OBSERVATIONS

A few small solar flares occurred on the Sun between 11:45 UT and 14:40 UT on 2014 July 07. They were detected by the space-based instruments in multi-wavelengths, whose details are listed in table 1. During solar flares, SDO/AIA usually has two different exposure times, i.e., one short exposure followed by one long exposure. The long-exposure observations can increase the signal-to-noise ratio, however, they can also result in image saturation, in particular during a strong flare. Therefore, to avoid the effect of image saturation, we here only use images with short exposures, which means that the time cadence of AIA images in EUV wavelengths is reduced to 24 s (Lemen et al., 2012; Ning, 2017).

Figure 1 shows the normalized light curves integrated over the whole Sun at multiple wavelengths detected by the SDO/EVE, GOES, and SDO/AIA, respectively. Here, the light curves measured by the EVE and AIA are normalized by the equation $\frac{I - I_{min}}{I_{max} - I_{min}}$, where I is the observed intensities, I_{min} and I_{max} represent the minimum and maximum intensities, respectively. The light curves in panel (a) were obtained from the EUV SpectroPhotometer (ESP, Didkovsky et al., 2012) onboard SDO/EVE. It can be seen that the SXR light curve in ESP 1–70 Å exhibits several peaks, such as peaks 1–4. Then the similar peaks can be found in the EUV flux at ESP 300 Å, which is a bit earlier than the SXR peaks. Moreover, the first three peaks (1–3) at ESP 300 Å is much smaller than the last one (4), which is the weakest peak at ESP 1–70 Å. On the other hand, only the last peak could be easily identified in the EUV irradiance at ESP 180 Å. The ESP 180 Å channel contains line emissions that mainly come from the plasmas around 1–2 MK, while the ESP 260 Å and 300 Å channels are dominated by He II lines (Didkovsky et al., 2012; Woods et al., 2012).

Figure 1 (b) presents the GOES flux in SXR 1–8 Å (red) and 0.5–4 Å (blue), from which, we can find the similar peaks to the ESP SXR light curve, as indicated by 1–4. Thus, those four peaks can be identified as the C-class flare. Moreover, they exhibit impulsive peaks in the temperature profile derived from the GOES fluxes using the isothermal assumption (White et al., 2005), which are consistent with the SXR flare peaks, indicating these four flares are hot. Therefore, these four flares display almost the same evolutionary behavior in the SXR flux recorded by the GOES and EVE/ESP. Finally, the radio spectrogram shows a strong and well-developed type III burst at frequencies between ~0.1 MHz and ~16 MHz during the flare ‘4’, as shown in the context image measured by the SWAVES.

To confirm that the EUV flux recorded by the EVE/ESP is credible, we then plot the SDO/AIA light curves integrated over the full-disk Sun in EUV passbands, as shown in Figure 1 (c). The SDO/AIA fluxes in high (>6 MK) temperature channels exhibit the similar flare peaks as the SXR light curves, i.e., AIA 131 Å (~10 MK), and 94 Å (~6.3 MK), and the light curve in low (<0.1 MK) temperature channel also shows similar peaks with the ESP 300 Å flux, such as AIA 304 Å (~0.05 MK). The time delays among these light curves can be clearly seen in the first three flares, but not found in the last flare. On the other hand, the SDO/AIA fluxes in middle temperature (~0.6–2 MK) wavelengths such as AIA 211 Å (~2.0 MK), 193 Å (~1.6 MK), and 171 Å (~0.6 MK) only display the pronounced peak

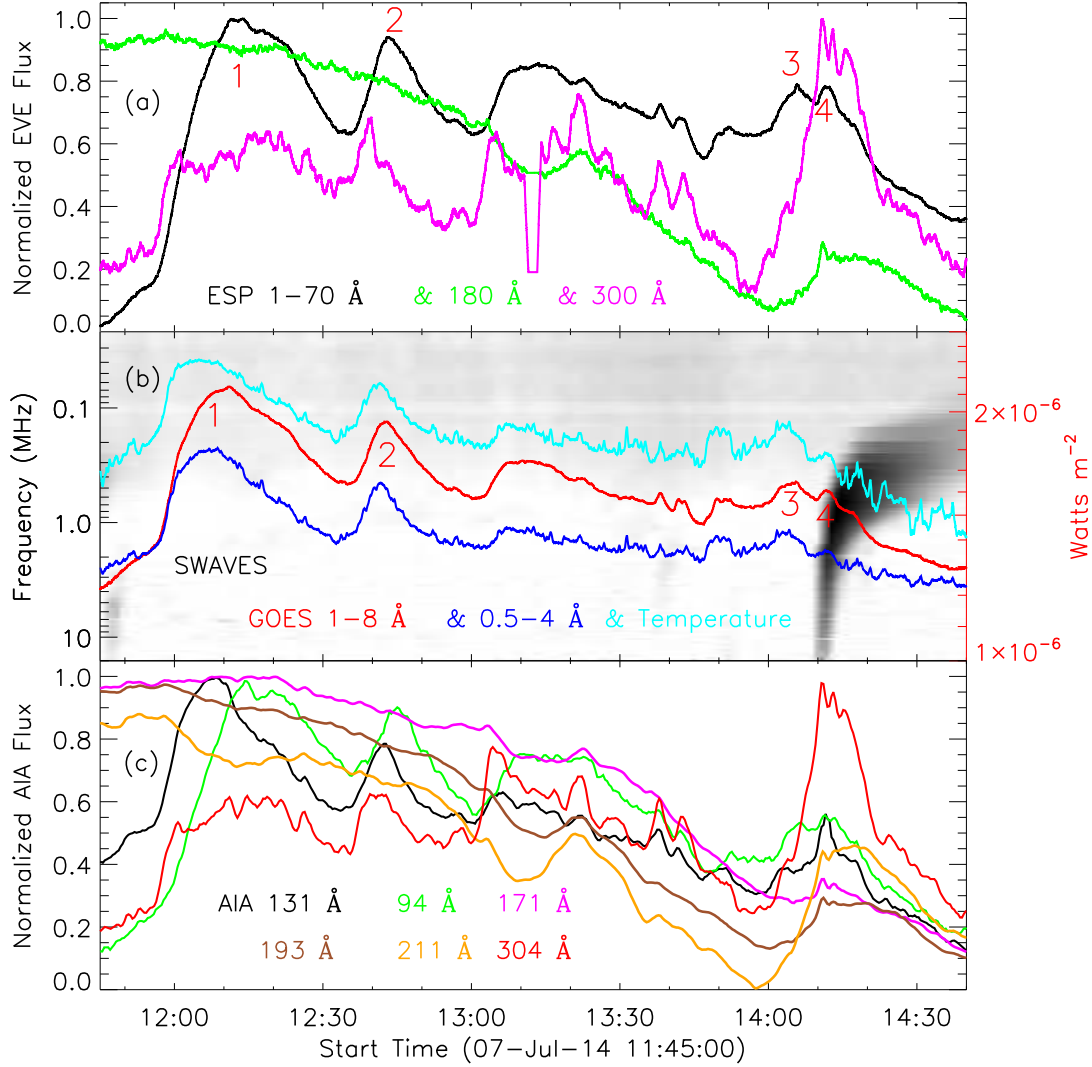


Fig. 1 Panel (a): Normalized SDO/EVE fluxes between 11:45 UT and 14:40 UT on 2014 July 07 in ESP 1–70 Å (black), 180 Å (green), and 300 Å (magenta). Panel (b): GOES fluxes in SXR 1–8 Å (red) and 0.5–4 Å (blue), and temperature (cyan). Panel (c): Normalized light curves integrated over the full-disk Sun in AIA 131 Å (black), 94 Å (green), 171 Å (magenta), 193 Å (brown), 211 Å (orange), and 304 Å (red). The context image in panel (b) is radio spectrogram derived from SWAVES.

for the flare 4, which are almost simultaneous. This observational result is consistent with EVE/ESP observations at different channels.

3 RESULTS

For further analysis, four flare subregions, which are the source regions of the solar flares under study, are selected. These subregions are marked with the red rectangles in Figure 2, and each of them is

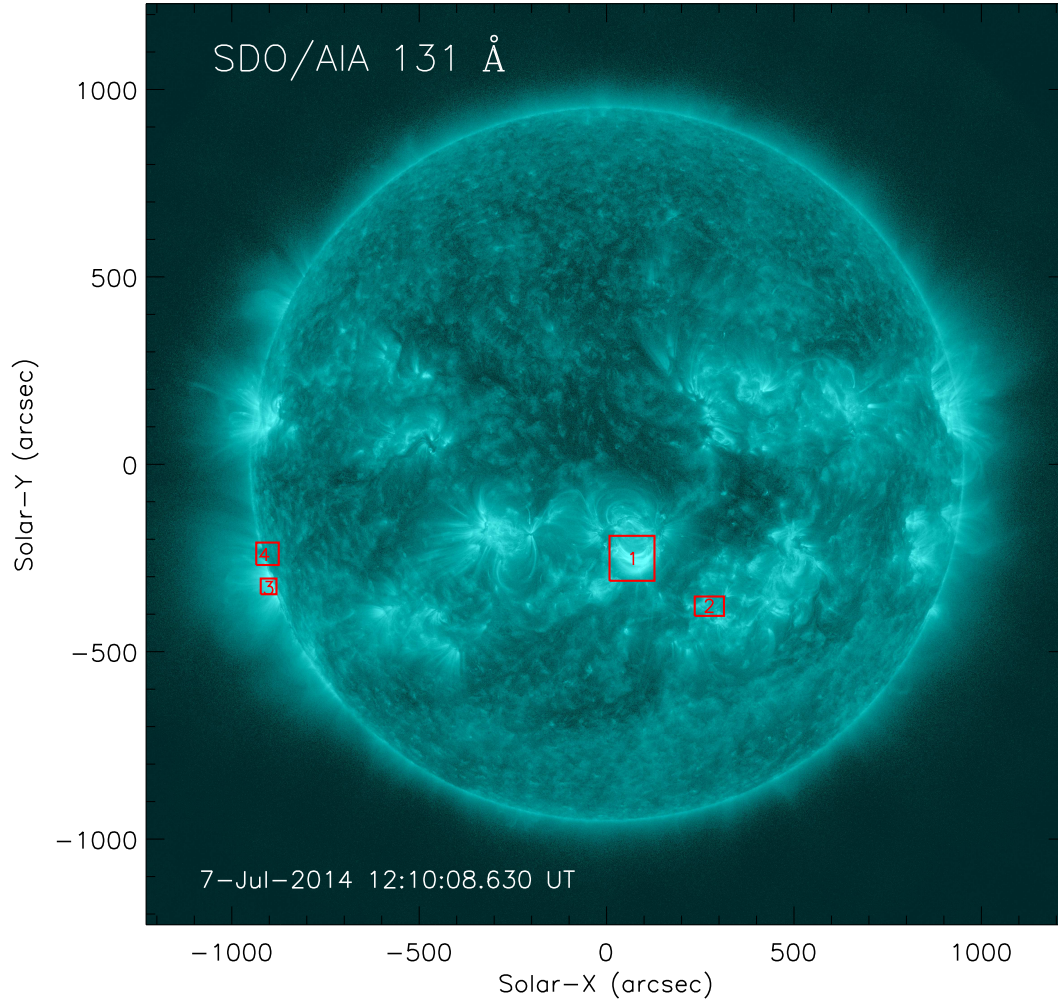


Fig. 2 Snapshot of the full Sun in AIA 131 Å at 12:10:08 UT on 2014 July 07. The red rectangles indicate the flare subregions in this study.

assigned a number. Two of the flare regions numbered by ‘1’ and ‘2’ are located near the solar disk center, while the other two (‘3’ and ‘4’) are located at the solar limb. Figure 3 shows the normalized fluxes resulting from an integration of the SDO/AIA images over the subregions for flares 1 and 4. As can be seen in panel (a), the flare 1 exhibits a pronounced peak in both high and low temperature EUV channels, and the peak time of AIA 304 Å is a little earlier than that of AIA 131 Å and 94 Å. Moreover, they decay slowly and can maintain a long time. This flare shows a weak peak during the impulsive phase of solar flare in the middle temperature EUV channels, such as AIA 335 Å, 211 Å, 193 Å and 171 Å, which is almost at the same time with that in AIA 304 Å. On the other hand, the strong peak in the middle temperature EUV channels is seen during the flare decay phase, which could be considered as the post flare loops, as can be seen in the movie of flare1.mp4. The strong peaks both in

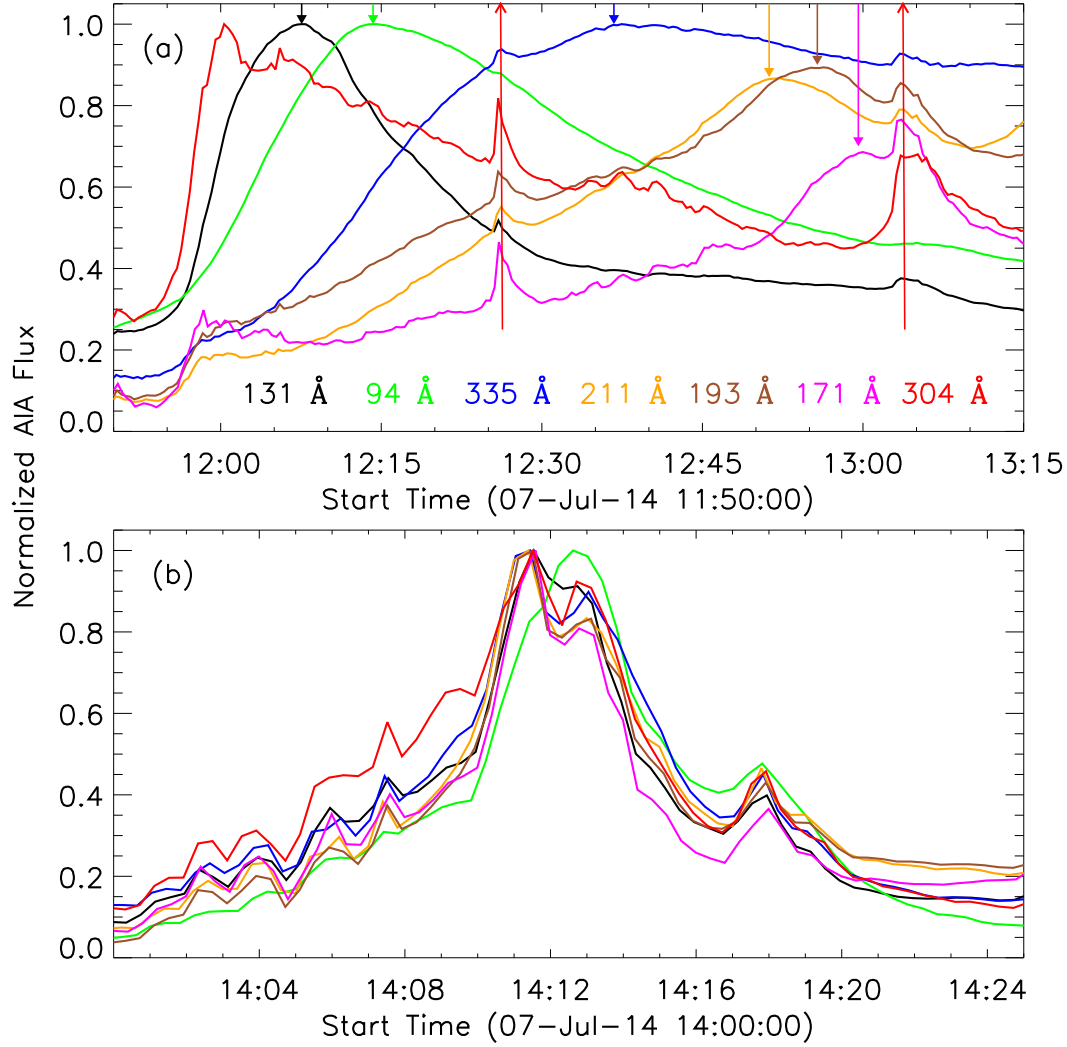


Fig. 3 Normalized EUV fluxes for flares 1 and 4 at wavelengths of AIA 131 Å (black), 94 Å (green), 335 Å (blue), 211 Å (orange), 193 Å (brown), 171 Å (magenta), and 304 Å (red) derived from the flare subregions outlined by the red rectangles in Figure 2. The red arrows indicate the small jets, while the other color arrows marks the peak time at multiple wavelengths.

high and middle temperature EUV channels appear subsequently, as indicated by the solid color arrows. All these observational facts suggest a slowly cooling precess in this flare. Panel (b) shows that the flare 4 emits strongly radiation at almost all the SDO/AIA wavebands, including the high, middle and low temperature channels. Moreover, the flare emission in different channels reach the peaks at almost the same time. Then, it decays quickly and has a short lifetime in all EUV wavelengths. In a word, it releases energy drastically and quickly in all the observed wavelengths. In addition, the flare peaks in

flares 2 and 3 also appear subsequently in different EUV wavelengths, as shown in Figure A.1, which are similar to flare 1.

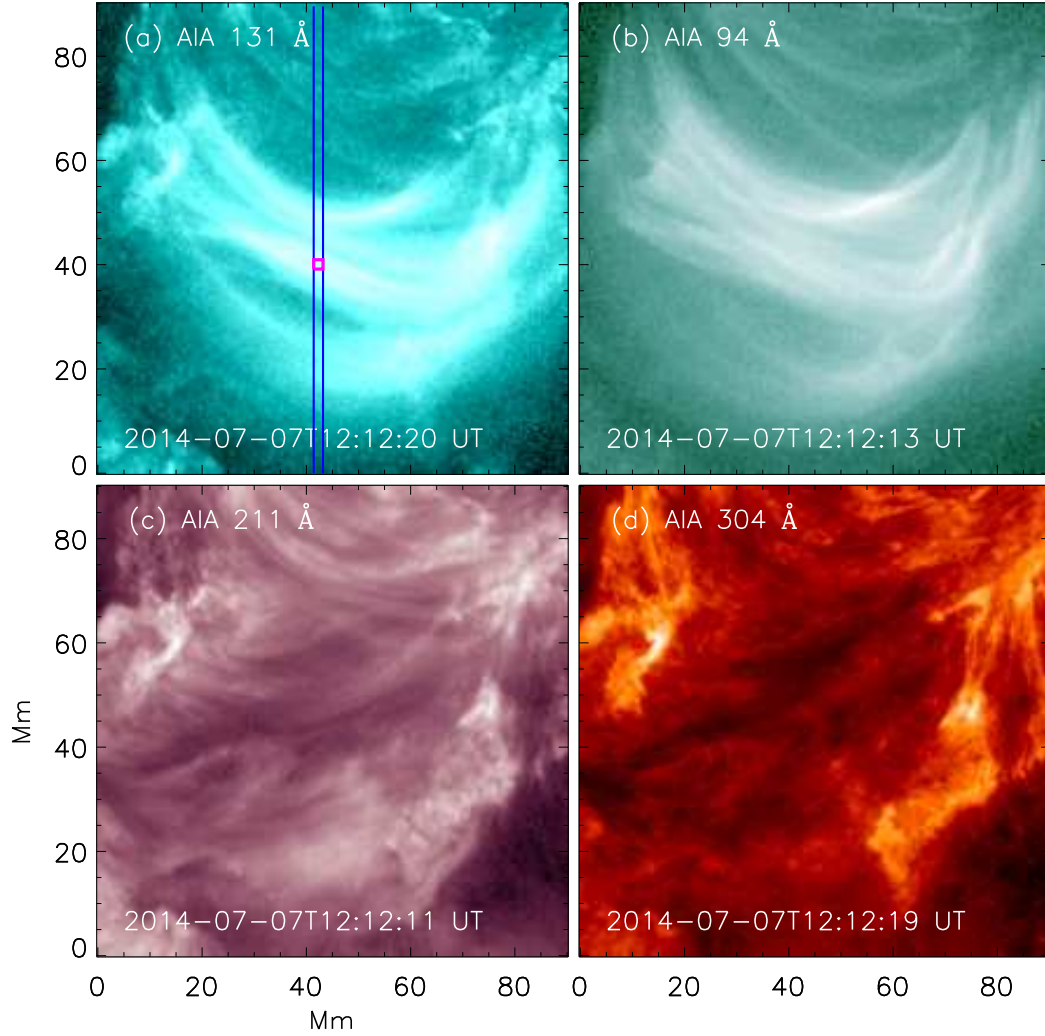


Fig. 4 Small FOV images for flare 1 at around 12:12 UT in AIA 131 Å (a), and 94 Å (b), 211 Å (c) and 304 Å (d). The magenta box outlines the flare loop region ($2.4'' \times 2.4''$) used to perform the DEM analysis, and double blue lines outline the positions used to integrate the intensities along the north-south direction.

To look closely the geometries of these flares, we then plot the AIA images with a small field-of-view (FOV) during flare peak times. Figure 4 shows SDO/AIA images in EUV wavelengths for the flare 1 with a FOV of about $90 \times 90 \text{ Mm}^2$, as outlined by the red box '1' in Figure 2. Panel (a) and (b) presents the small FOV images in AIA 131 Å and 94 Å at a time about 12:12 UT, which is around the peak time of flare 1 in GOES 1–8 Å (Figure 1) and AIA 94 Å (Figure 3). We can clearly see a broad bundle of flare loops in these two high temperature EUV wavelengths. However, it is a combination of

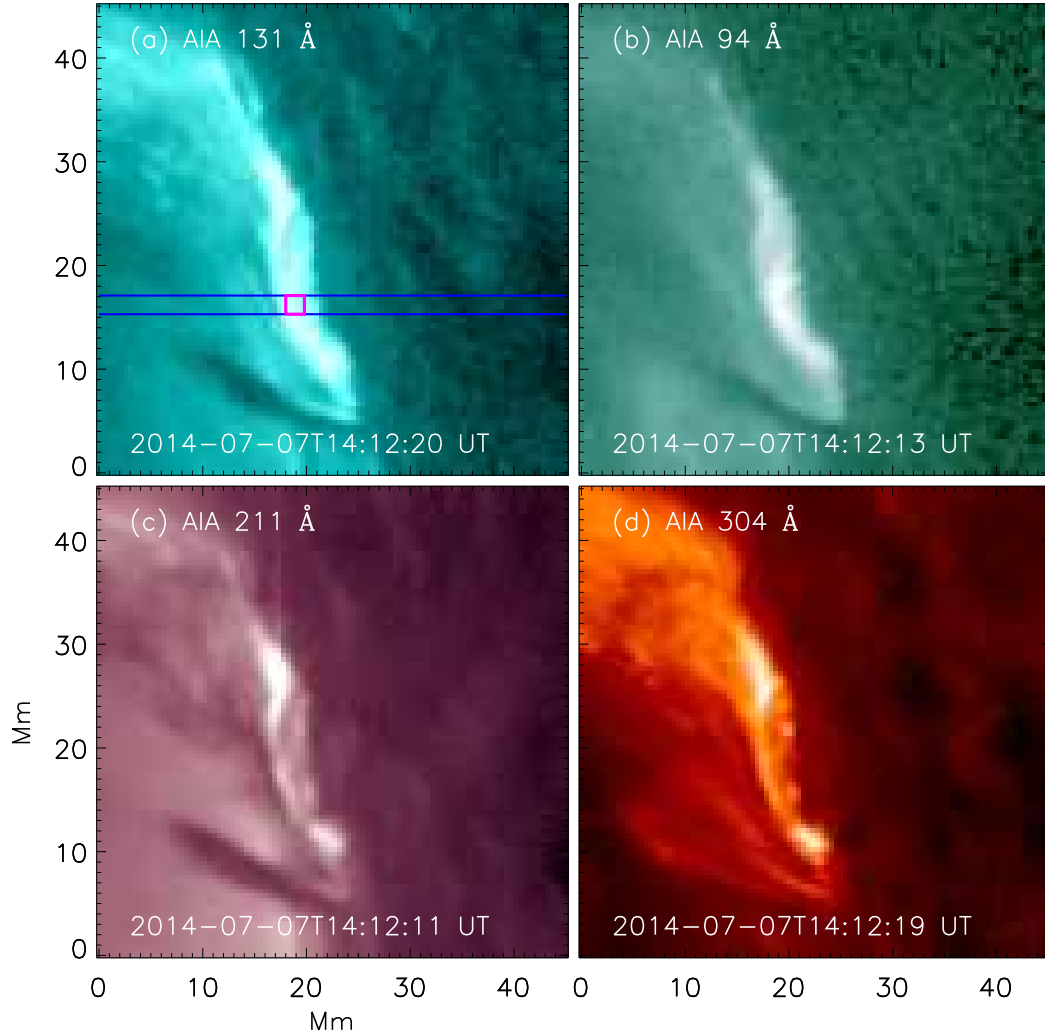


Fig. 5 Same as Figure 4, but for flare 4 at around 14:12 UT.

the limited spatial resolution of AIA and the simple fact that multiple optically thin loops overlaid on each other just cannot be easily separated. Therefore, we consider them together and use a Gaussian function to fit them, which are integrated along two blue lines in panel (a). Thus, we estimate a loop thickness of about 13.6 Mm, which is regarded as the full width at half maximum (FWHM). Then, panels (c) and (d) display the same FOV images in AIA 211 Å and 304 Å at almost the same time i.e., around 12:12 UT. From which, we can see two weak flare ribbons, implying that the flare emission in these two EUV wavelengths mainly appears in the ribbons during the impulsive phase. The flare loops, on the other hand, could not be seen in these middle temperature AIA wavelengths at impulsive and main phases that close to the flare peak time. All these AIA images suggests that the diffuse flare loops in the high temperature channels connect double ribbons seen in middle and low temperature wavelengths. The movie of flare1.mp4 suggests that the flare 1 is constituted of strong hot loops but weak ribbons

at impulsive and main phases. Finally, at the decay phase that far away from the flare peak time, some post flare loops (Li & Zhang, 2009; Li et al., 2009) can be found subsequently. We would like to point out that these post flare loops appear successively, suggesting a cooling process during this flare. We also notice that some small peaks appear at around 12:26 UT and 13:02 UT (red arrows) at all the EUV channels in Figure 3 (a), which are from two small-scale jets, as shown in the movie of flare1.mp4.

For flare 4 which is located at the solar limb, Figure 5 shows the AIA images at a time near 14:12 UT with a small FOV of around $45 \times 45 \text{ Mm}^2$, as marked by the red box '4' in Figure 2. These images and the movie of flare4.mp4 show that flare 4 is very compact and emits radiation in all the EUV wavelengths. This flare is associated with a small-scale filament eruption, as can be seen in the movie. It also causes a solar jet and leads to a weak CME (see detail in Lu et al., 2019), as well as a type III radio burst (Figure 1 b). Using the same Gaussian fit method for the intensities integrated along two blue lines in panel (a), we then estimate the loop thickness (i.e., FWHM) of $\sim 2.2 \text{ Mm}$. Figures B.1 and B.2 show the AIA images at around 12:44 UT and 14:01 UT for flares 2 and 3, respectively. The subregions considered here have sizes of $58 \times 39 \text{ Mm}^2$ and $32 \times 32 \text{ Mm}^2$, respectively. These images present a similar analysis for flares 2 and 3, both of which show a consistent result with the flare 1. In other words, they are constituted of bright hot loops but faint ribbons with low temperature at impulsive and main phases that close to the flare peak time. In the decay phase, the flare loops appear successively at different EUV channels. Note that this characteristic is independent of the flare location on the disk, so it can not be explained by projection effects.

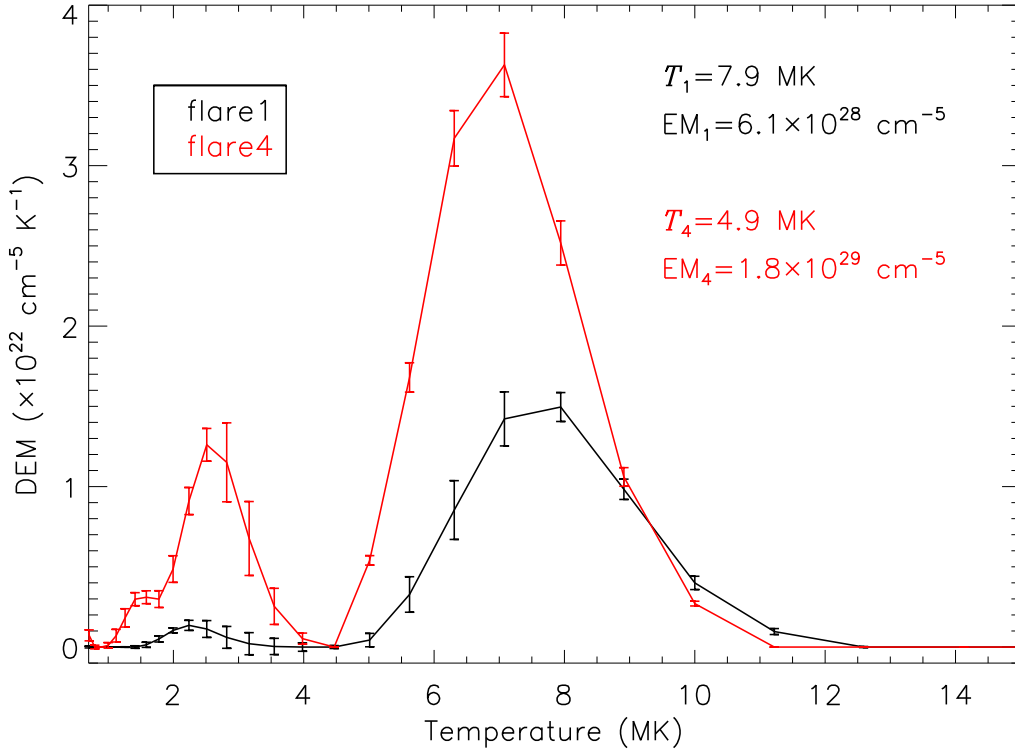


Fig. 6 DEM curves at the selected positions (magenta box) for flare 1 (black) and flare 4 (red). The error bars are estimated from the 100 MC simulations. The EM-weighted mean temperature and total EM are given.

In order to determine the electron number density (n) in the flare regions, we perform a differential emission measure (DEM) analysis using observations made in six AIA EUV wavelengths. We employ the sparse inversion code by Cheung et al. (2015) in a recently modified version (Su et al., 2018), and the DEM uncertainties are estimated from 100 Monte Carlo (MC) simulations, i.e., their standard deviation. Assuming optically thin emissions in solar flares, the total emission measure (EM) and the EM-weighted mean temperature (T) in the selected flare regions can be derived from the DEM results. Figure 6 presents the DEM curves at the selected positions (magenta box), where flare emissions in high temperature channels are strongest. It can be seen that the flare 1 (black) shows a strong peak at the higher temperature of around 8 MK, suggesting hot loops in flare 1 during the impulsive phase. On the other hand, the flare 4 (red) displays double peaks at the higher (~ 7 MK) and lower (~ 2.5 MK) temperatures, implying multi-thermal structures in this flare. Then, the electron number density is calculated according to $n = \sqrt{\frac{EM}{w}}$ (see, Aschwanden, 2005), where w represents the effective line-of-sight (LOS) depth, which is adopted as the loop thickness here. We can estimate the EM-weighted mean temperature and electron number density at a small region (magenta box) for flares 1 and 4, such as $T_1 = 7.9$ MK, $T_4 = 4.9$ MK, $n_1 = 6.7 \times 10^9 \text{ cm}^{-3}$, $n_4 = 2.9 \times 10^{10} \text{ cm}^{-3}$, respectively. It can be seen that flare 4 has a larger number density but a lower temperature compared to flare 1, indicating that flare 4 is denser but cooler than the first flare.

4 CONCLUSION AND DISCUSSION

Using multiple-wavelength observations measured by SDO/EVE, SDO/AIA, GOES, and SWAVES, four solar flares occurring on 2014 July 07 were studied. They all emitted thermal radiation generated by hot plasma in SXR wavelengths, i.e., ESP 1–70 Å, GOES 1–8 Å, and 0.5–4 Å. The first three flares (flares 1–3) showed strong emissions in SXR and high temperature EUV wavelengths during the impulsive phase, and no radio burst was detected. Moreover, they could maintain a long lifetime. During their decay phases that far away from the flare peak time, some post flare loops appear subsequently at the middle temperature channels, such as AIA 335 Å, 211 Å, 193 Å and 171 Å, suggesting long cooling time from high to low temperatures. Conversely, the last flare (flare 4) in our samples was emitting simultaneously in almost all the SXR and EUV channels and was accompanied by a strong type III radio burst, and it was fade quite quickly. We stress that the bright emissions in EUV wavelengths could reach peaks at almost the same time, which is most likely to be an erupting filament.

The reason why the first three flares are different from the last one is most likely associated with their geometric configurations (Zhang et al., 2017; Sarkar & Srivastava, 2018). The first three flares show very diffuse loops in high temperature channels at beginning, and then appear subsequently in other EUV wavebands, while the flare 4 exhibits a compact feature in all EUV wavelengths. For the first three flares, magnetic reconnection might be triggered by the interactions of hot flare loops at beginning (see, Török & Kliem, 2005; Guo et al., 2010; Liu et al., 2014). In these events, the lack of emission from low/middle temperature plasmas is found during the impulsive phase, i.e., before the peak of SXR flux. However, the appearance of flare ribbons and post flare loops in the middle temperature channels support the energy transport from the reconnection region to the chromosphere and the occurrence of chromospheric evaporation during these flares, which is similar to particle acceleration with subsequent chromospheric evaporation (e.g., Fisher et al., 1985; Milligan, 2015; Brosius et al., 2016; Tian & Chen, 2018). On the other hand, the lower number density and longer flare loops should imply smaller radiative and conductive losses, which would result in a significantly longer cooling time as compared to the last event (Cargill et al., 1995; Aschwanden, & Alexander, 2001; Benz, 2017). The bulk of the released energy will thus be retained in flare loops for a long duration, while comparatively little energy will be slowly transported to the deeper atmospheric layers. This is also consistent with the subsequent post flare loops at middle temperature channels, which are far away from the flare peak time. Conversely, flare 4 has high density, resulting in larger radiative losses – a possible mechanism for energy transport to deeper layers. This is confirmed by the DEM results during the flare peak time, which show hot temperatures but low densities in flare 1, and a multi-thermal temperature but high density in flare 4.

We would like to point out that the first three flares might be caused by the reconnection between complex hot flare loops, so there is no open field line generated during the flare processes. Thus, there is no type III radio burst during these three flares, which is also the difference of the first three flares from the last flare associated with the filament eruption. On the other hand, the flare 4 is associated with an erupting filament, the accelerated electron beams then propagate upward along the open magnetic field lines, generating the type III radio burst. Unfortunately, no appropriate HXR observations were available for our event sample, so we cannot make a definite conclusion about the role of energetic electrons. To make this conclusion more robust, we will investigate more cases which will include explicit HXR observations in future, since they provide direct evidences of nonthermal electrons in the low solar atmosphere (Fletcher et al., 2011; Benz, 2017). The Hard X-ray Imager (Su et al., 2019; Zhang et al., 2019) on board Advanced Space-based Solar Observatory (Gan et al., 2019; Huang et al., 2019) and the Spectrometer/Telescope for Imaging X-rays (Krucker et al., 2020) aboard Solar Orbiter (Müller et al., 2013) could help to solve this problem, in particular for their joint observations in HXR channels (e.g., Krucker et al., 2019).

It is worthwhile to stress that the first three flares are geometrically quite extended, — in particular compared to flare 4. Taking the flare 1 for example, the double footpoints connected by flare loops are separated by $s \sim 70$ Mm, which corresponds to some of the largest values of the RHESSI flares found by Warmuth & Mann (2013). Considering optically thin emissions in solar flares, the broad bundle of flare loops should correspond to a large LOS depth (d), thus resulting in low densities and therefore a low radiative cooling rate. Conversely, when the loop half-length ($L \approx \pi s/4$) is adopted at the thermal gradient length, a comparatively low conductive cooling rate would result. Using the key parameters derived from flare 1, such as the number density (n_1), the plasma temperature (T_1), and loop half-length (L), the conductive cooling (τ_{con}) and radiative cooling (τ_r) timescales (cf. Cargill & Klimchuk, 2004; Reale, 2014) could be estimated, which are $\tau_{con} \sim 29$ minutes and $\tau_r \sim 166$ minutes, respectively. Similarly, the conductive cooling (τ'_{con}) and radiative cooling (τ'_r) timescales of flare 4 can also be estimated from its key parameters, such as $\tau'_{con} \sim 44$ minutes and $\tau'_r \sim 19$ minutes. It should be mentioned that the role of conduction is still under discussion. There are theoretical arguments that suggest conduction might be significantly suppressed in solar flares (e.g., Bian et al., 2018; Emslie & Bian, 2018, and references therein). Conversely, there is evidence for conductive evaporation in some events (e.g., Battaglia et al., 2009; Zhang & Ji, 2013). In general, shorter flare loops should lead to smaller conductive timescales (Aschwanden, & Alexander, 2001), but in our case (flare 4) this is overcompensated by the multi-thermal temperature. The conductive timescales are comparable in our flares, so conduction is not favored for the explanation of the vastly different decay timescales. In other words, our interpretation does not depend on the exact role of conduction: the vastly different radiative cooling timescales are sufficient for explaining the different temporal evolution of the compact flare 4 as opposed to the extended flares 1–3.

It is also necessary to stress that the long lifetime of the first three flares is essentially distinct from the EUV late phase of solar flares discovered by SDO/EVE and SDO/AIA, which refers to the second peak in warm EUV (i.e., Fe XVI 335 Å) channels (Woods et al., 2011; Woods, 2014). Since the first three flares in our work do not exhibit the second large peak which is separated from the impulsive peak in high temperature EUV wavelengths, such as AIA 131 Å and 94 Å. Moreover, the middle temperature EUV (e.g., AIA 335 Å, 211 Å, 193 Å and 171 Å) channels show peak successively in our flares, as can be seen in Figure 3.

Acknowledgements We acknowledge the anonymous referee for his/her valuable comments. We thank the teams of SDO/EVE, SDO/AIA, GOES, and STEREO for their open data use policy. This work is supported by NSFC under grants 11973092, 11790300, 11790302, 11729301, 11603077, and the Strategic Priority Research Program on Space Science, CAS, Grant No. XDA15052200 and XDA15320301. D. Li is also supported by the Specialized Research Fund for State Key Laboratories and CAS Strategic Pioneer Program on Space Science (KLSA202003). The Laboratory No. 2010DP173032. The work of A. W. was supported by DLR under grant No. 50 QL 1701.

References

- Asai, A., Nakajima, H., Shimojo, M., et al. 2006, PASJ, 58, L1
- Aschwanden, M. J., & Alexander, D. 2001, Sol. Phys., 204, 91
- Aschwanden, M. J. 2005, Physics of the Solar Corona (2nd ed.; Chichester: Praxis Publishing), P69
- Battaglia, M., Fletcher, L., & Benz, A. O. 2009, A&A, 498, 891
- Benz, A. O. 2017, Living Reviews in Solar Physics, 14, 2
- Bian, N., Emslie, A. G., Horne, D., & Kontar, E. P. 2018, ApJ, 852, 127
- Brosius, J. W., Daw, A. N., & Inglis, A. R. 2016, ApJ, 830, 101
- Carmichael, H. 1964, NASA Special Publication, 50, 451
- Cargill, P. J., Mariska, J. T., & Antiochos, S. K. 1995, ApJ, 439, 1034
- Cargill, P. J., & Klimchuk, J. A. 2004, ApJ, 605, 911
- Chen, Y., Wu, Z., Liu, W., et al. 2017, ApJ, 843, 8
- Chen, B., Shen, C., Gary, D. E., et al. 2020, Nature Astronomy, doi:10.1038/s41550-020-1147-7
- Cheng, X., Kliem, B., & Ding, M. D. 2018, ApJ, 856, 48
- Cheung, M. C. M., Boerner, P., Schrijver, C. J., et al. 2015, ApJ, 807, 143
- Dai, Y., Ding, M. D., & Guo, Y. 2013, ApJ, 773, L21
- Didkovsky, L., Judge, D., Wieman, S., Woods, T., & Jones, A. 2012, Sol. Phys., 275, 179
- Emslie, A. G., & Bian, N. H. 2018, ApJ, 865, 67
- Fan, Y., & Gibson, S. E. 2007, ApJ, 668, 1232
- Fisher, G. H., Canfield, R. C., & McClymont, A. N. 1985, ApJ, 289, 414
- Fletcher, L., & Hudson, H. S. 2002, Sol. Phys., 210, 307
- Fletcher, L., Dennis, B. R., Hudson, H. S., et al. 2011, Space Sci. Rev., 159, 19
- Forbes, T. G., Linker, J. A., Chen, J., et al. 2006, Space Sci. Rev., 123, 251
- Gan, W. Q., Zhu, C., Deng, Y. Y., et al. 2019, Research in Astronomy and Astrophysics, 19, 156
- Guo, Y., Ding, M. D., Schmieder, B., et al. 2010, ApJ, 725, L38
- Hirayama, T. 1974, Sol. Phys., 34, 323
- Hoyng, P., Duijveman, A., Machado, M. E., et al. 1981, ApJ, 246, L155
- Huang, Y., Li, H., Gan, W. Q., et al. 2019, Research in Astronomy and Astrophysics, 19, 164
- Ji, H., Wang, H., Schmahl, E. J., Moon, Y. J., & Jiang, Y. 2003, ApJ, 595, L135
- Kaiser, M. L., Kucera, T. A., Davila, J. M., et al. 2008, Space Sci. Rev., 136, 5
- Kopp, R. A., & Pneuman, G. W. 1976, Sol. Phys., 50, 85
- Krucker, S., Battaglia, M., Cargill, P. J., et al. 2008, A&A Rev., 16, 155
- Krucker, S., Hurford, G. J., Su, Y., et al. 2019, Research in Astronomy and Astrophysics, 19, 167
- Krucker S., et al., 2020, A&A, in press
- Lemen, J. R., Title, A. M., Akin, D. J., et al. 2012, Sol. Phys., 275, 17
- Li, L., & Zhang, J. 2009, ApJ, 690, 347
- Li, L., Duan, H., & Zhang, J. 2009, Science in China: Physics, Mechanics and Astronomy, 52, 1723
- Li, L., Zhang, J., Peter, H., et al. 2016, Nature Physics, 12, 847
- Li, T., Zhang, J., & Hou, Y. 2017a, ApJ, 848, 32
- Li, Y., Ding, M. D., Guo, Y., & Dai, Y. 2014, ApJ, 793, 85
- Li, Y., Kelly, M., Ding, M. D., et al. 2017b, ApJ, 848, 118
- Li, D. 2019, Research in Astronomy and Astrophysics, 19, 067
- Lin, J. 2004, Sol. Phys., 219, 169
- Lin, J., Ko, Y. K., Sui, L., et al. 2005, ApJ, 622, 1251
- Lin, R. P., Krucker, S., Hurford, G. J., et al. 2003, ApJ, 595, L69
- Liu, W., Chen, Q., & Petrosian, V. 2013, ApJ, 767, 168
- Liu, R., Titov, V. S., Gou, T., et al. 2014, ApJ, 790, 8
- Liu, K., Wang, Y., Zhang, J., et al. 2015, ApJ, 802, 35
- Lu, L., Feng, L., Li, Y., et al. 2019, ApJ, 887, 154
- Mann, G., & Warmuth, A. 2011, A&A, 528, A104
- Masuda, S., Kosugi, T., Hara, H., Tsuneta, S., & Ogawara, Y. 1994, Nature, 371, 495

- Milligan, R. O. 2015, *Sol. Phys.*, 290, 3399
- Müller, D., Marsden, R. G., St. Cyr, O. C., et al. 2013, *Sol. Phys.*, 285, 25
- Ning, Z. 2017, *Sol. Phys.*, 292, 11
- Ning, Zongjun, Li, Dong & Zhang, Qingmin, 2020, *Research in Astronomy and Astrophysics*, 9, 138
- Ohki, K., Takakura, T., Tsuneta, S., & Nitta, N. 1983, *Sol. Phys.*, 86, 301
- Pallavicini, R., Serio, S., & Vaiana, G. S. 1977, *ApJ*, 216, 108
- Priest, E., & Forbes, T. 2000, *Magnetic reconnection : MHD theory and applications* / Eric Priest, Terry Forbes. New York : Cambridge University Press, 2000.,
- Priest, E. R., & Forbes, T. G. 2002, *A&A Rev.*, 10, 313
- Qiu, J., Gary, D. E., & Fleishman, G. D. 2009, *Sol. Phys.*, 255, 107
- Radziszewski, K., Rudawy, P., & Phillips, K. J. H. 2007, *A&A*, 461, 303
- Reale, F. 2014, *Living Reviews in Solar Physics*, 11, 4
- Saint-Hilaire, P., & Benz, A. O. 2002, *Sol. Phys.*, 210, 287
- Sarkar, R., & Srivastava, N. 2018, *Sol. Phys.*, 293, 16
- Shen, Y. D., Liu, Y., & Liu, R. 2011, *Research in Astronomy and Astrophysics*, 11, 594
- Shibata, K., Masuda, S., Shimojo, M., et al. 1995, *ApJ*, 451, L83
- Shibata, K., & Magara, T. 2011, *Living Reviews in Solar Physics*, 8, 6
- Sturrock, P. A., & Coppi, B. 1964, *Nature*, 204, 61
- Sturrock, P. A. 1966, *Nature*, 211, 695
- Song, Y. L., Guo, Y., Tian, H., et al. 2018, *ApJ*, 854, 64
- Su, Y., Golub, L., & Van Ballegooijen, A. A. 2007, *ApJ*, 655, 606
- Su, Y., Veronig, A. M., Holman, G. D., et al. 2013, *Nature Physics*, 9, 489
- Su, Y., Veronig, A. M., Hannah, I. G., et al. 2018, *ApJ*, 856, L17
- Su, Y., Liu, W., Li, Y. P., et al. 2019, *Research in Astronomy and Astrophysics*, 19, 163
- Sui, L., & Holman, G. D. 2003, *ApJ*, 596, L251
- Svestka, Z., & Cliver, E. W. 1992, *IAU Colloq. 133: Eruptive Solar Flares*, 399, 1
- Temmer, M., Veronig, A. M., Vršnak, B., & Miklenic, C. 2007, *ApJ*, 654, 665
- Thomas, R. J., & Teske, R. G. 1971, *Sol. Phys.*, 16, 431
- Tian, H., & Chen, N. H. 2018, *ApJ*, 856, 34
- Török, T., & Kliem, B. 2005, *ApJ*, 630, L97
- Wang, Y., & Zhang, J. 2007, *ApJ*, 665, 1428
- Wang, T., Sui, L., & Qiu, J. 2007, *ApJ*, 661, L207
- Wang, H., Liu, C., Deng, N., et al. 2014, *ApJ*, 781, L23
- Warmuth, A., & Mann, G. 2013, *A&A*, 552, A87
- Warmuth, A., & Mann, G. 2016, *A&A*, 588, A116
- White, S. M., Thomas, R. J., & Schwartz, R. A. 2005, *Sol. Phys.*, 227, 231
- Woods, T. N., Hock, R., Eparvier, F., et al. 2011, *ApJ*, 739, 59
- Woods, T. N., Eparvier, F. G., Hock, R., et al. 2012, *Sol. Phys.*, 275, 115
- Woods, T. N. 2014, *Sol. Phys.*, 289, 3391
- Xue, Z., Yan, X., Cheng, X., et al. 2016, *Nature Communications*, 7, 11837
- Yan, X. L., Yang, L. H., Xue, Z. K., et al. 2018, *ApJ*, 853, L18
- Yang, S., Zhang, J., & Xiang, Y. 2014, *ApJ*, 793, L28
- Zhang, J., Li, T., & Chen, H. 2017, *ApJ*, 845, 54
- Zhang, Q. M., Guo, Y., Chen, P.-F., et al. 2010, *Research in Astronomy and Astrophysics*, 10, 461
- Zhang, Q. M., & Ji, H. S. 2013, *A&A*, 557, L5
- Zhang, Q. M., Yang, S. H., Li, T., et al. 2020, *A&A*, 636, L11
- Zhang, Z., Chen, D.-Y., Wu, J., et al. 2019, *Research in Astronomy and Astrophysics*, 19, 160

Appendix A: AIA FLUXES FOR FLARES 2 AND 3

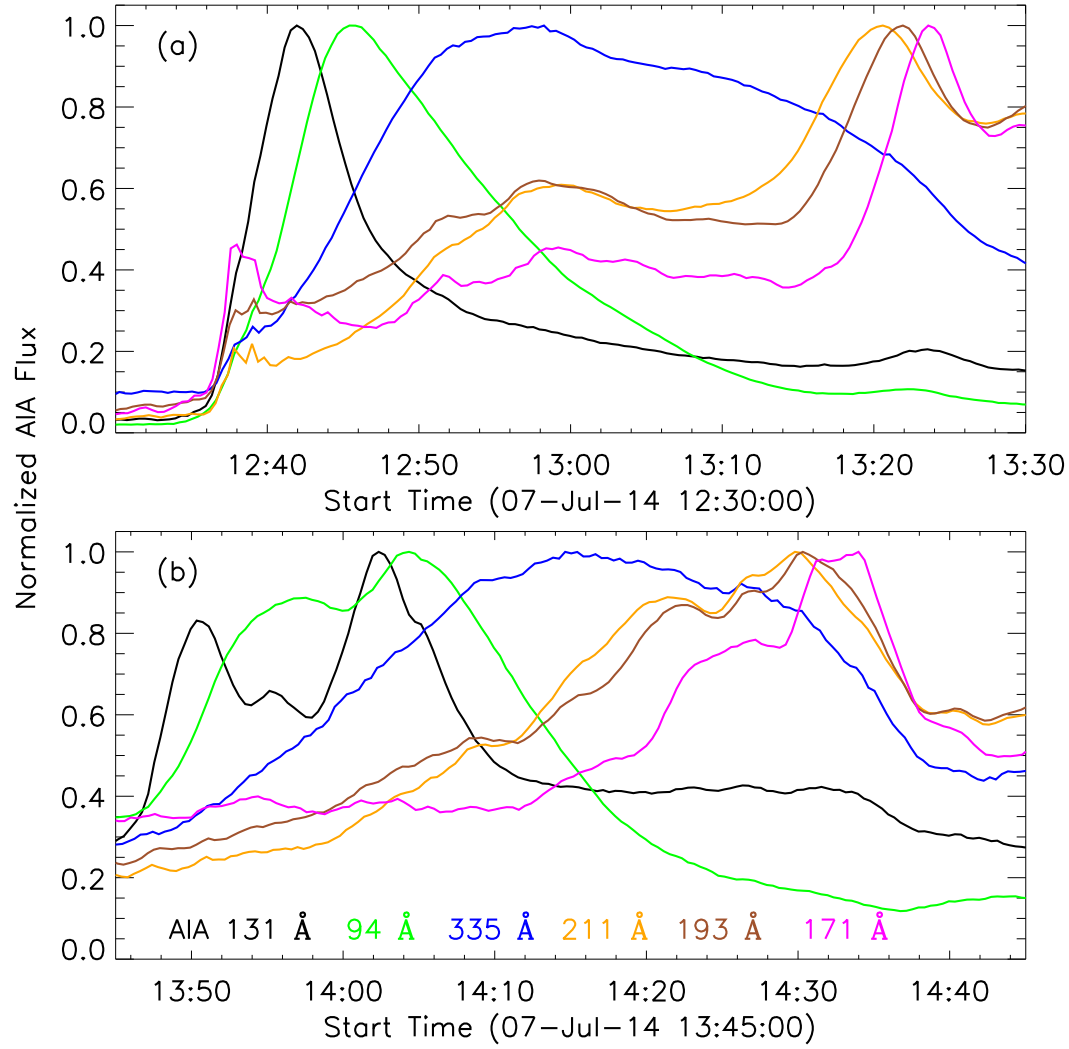


Fig. A.1 Normalized EUV fluxes for flares 2 and 3 at wavelengths of AIA 131 Å (black), 94 Å (green), 335 Å (blue), 211 Å (orange), 193 Å (brown), and 171 Å (magenta), which are derived from the flare subregions outlined by the red rectangles in Figure 2.

Appendix B: AIA IMAGES FOR FLARES 2 AND 3

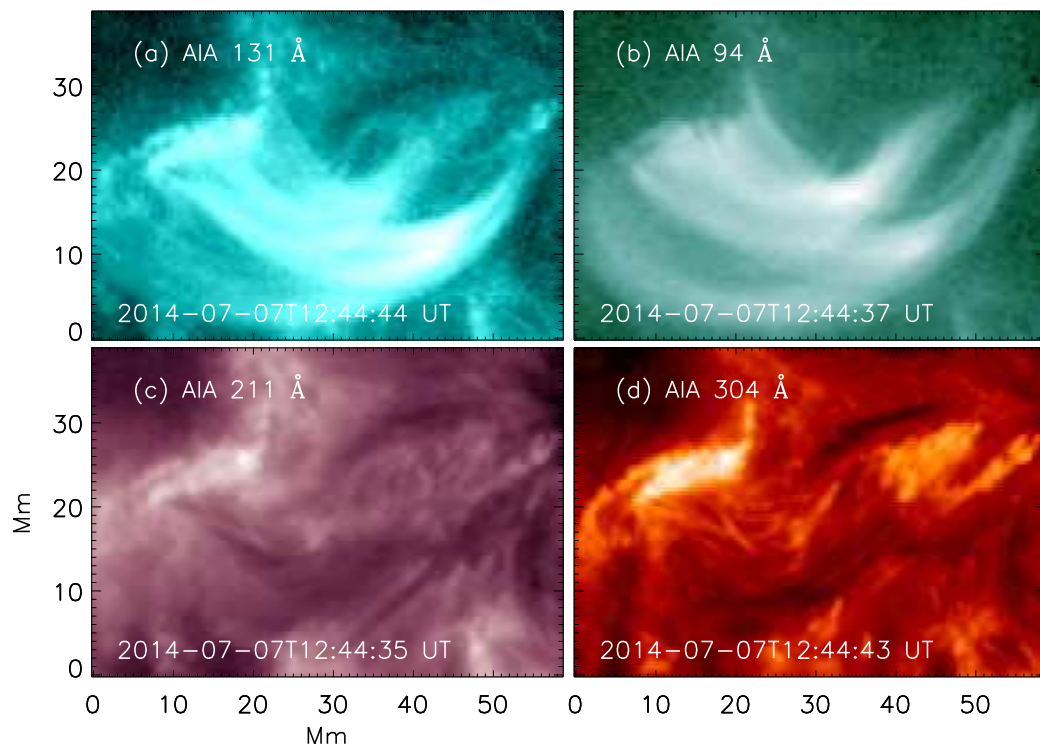


Fig. B.1 Small FOV images for flare 2 at around 12:44 UT in AIA 131 Å (a), 94 Å (b), 211 Å (c) and 304 Å (d).

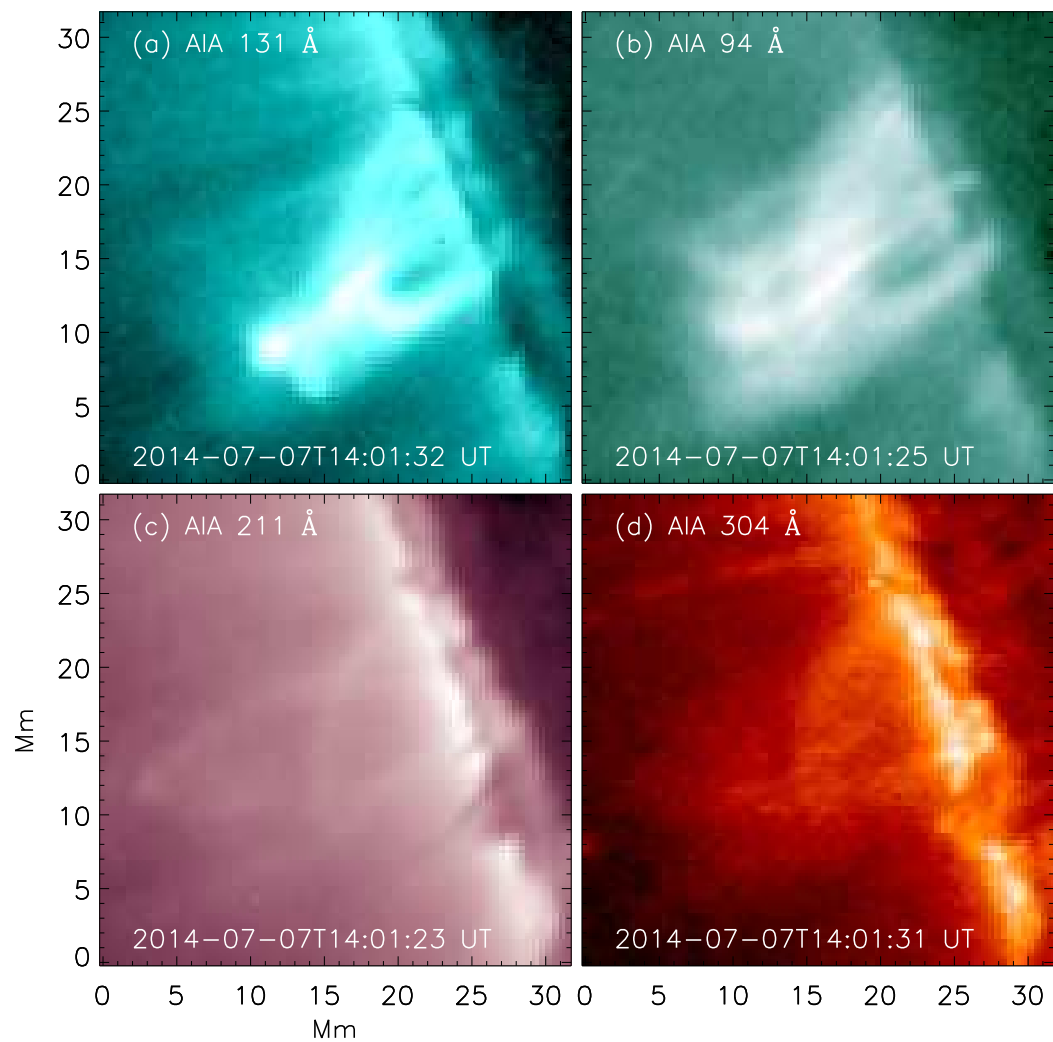


Fig. B.2 Same as Figure B.1, but for flare 3 at around 14:01 UT.